

# Stretch-induced wrinkling of polyethylene thin sheets: Experiments and modeling



Vishal Nayyar, K. Ravi-Chandar, Rui Huang<sup>\*</sup>

Department of Aerospace Engineering and Engineering Mechanics, University of Texas at Austin, Austin, TX 78712, United States

## ARTICLE INFO

### Article history:

Received 29 October 2013

Received in revised form 6 January 2014

Available online 6 February 2014

### Keywords:

Thin sheet

Buckling

Wrinkle

Viscoelasticity

## ABSTRACT

This paper presents a study on stretch-induced wrinkling of thin polyethylene sheets when subjected to uniaxial stretch with two clamped ends. Three-dimensional digital image correlation was used to measure the wrinkling deformation. It was observed that the wrinkle amplitude increased as the nominal strain increased up to around 10%, but then decreased at larger strain levels. This behavior is consistent with results of finite element simulations for a hyperelastic thin sheet reported previously (Nayyar et al., 2011). However, wrinkles in the polyethylene sheet were not fully flattened out at large strains (>30%) as predicted for the hyperelastic sheet, but exhibited a residual wrinkle whose amplitude depended on the loading rate. This is attributed to the viscoelastic response of the material. Two different viscoelastic models were adopted in finite element simulations to study the effects of viscoelasticity on wrinkling and to improve the agreement with the experiments, including residual wrinkles and rate dependence. It is found that a parallel network model of nonlinear viscoelasticity is suitable for simulating the constitutive behavior and stretch-induced wrinkling of the polyethylene sheets.

© 2014 Elsevier Ltd. All rights reserved.

## 1. Introduction

In a previous paper (Nayyar et al., 2011), we studied wrinkling of a rectangular hyperelastic thin sheet subjected to uniaxial stretch with two clamped ends (see Fig. 1) through finite element simulations. It was found that the formation of stretch-induced wrinkles depends on the applied nominal strain and two geometrical ratios, the length-to-width aspect ratio ( $\alpha = L_0/W_0$ ) and the width-to-thickness ratio ( $\beta = W_0/h_0$ ). The wrinkle wavelength was shown to decrease with increasing strain, in good agreement with a previous prediction using a scaling analysis (Cerdeja et al., 2002; Cerdeja and Mahadevan, 2003). However, the wrinkle amplitude was found to increase with strain until ~10% and then decrease, eventually flattening completely beyond a moderately large strain (~30%); in contrast, the scaling analysis predicted monotonically increasing wrinkle amplitude. Similar wrinkling problems have been studied by others, mostly using analytical or numerical methods (Segedin et al., 1988; Friedl et al., 2000; Jacques and Potier-Ferry, 2005; Zheng, 2009; Puntel et al., 2011; Kim et al., 2012; Healey et al., 2013). Very few experimental results have been reported (Cerdeja et al., 2002; Zheng, 2009). The experimental data in Cerdeja et al. (2002) showed that the measured wrinkle wavelengths in a polyethylene sheet agreed well with the

scaling analysis, but no data for the wrinkle amplitude was reported. Zheng (2009) measured stretch-induced wrinkle profiles in silicone membranes using an optical fringe projection method and found that the wrinkle amplitude decreased with increasing strain. The measurement however did not show increasing wrinkle amplitude at the early stage of stretching. In this paper, we present a detailed experimental study on stretch-induced wrinkling and then compare the results with numerical simulations assuming nonlinear elastic and viscoelastic material models. We note that experimental measurements of wrinkles have been reported by others for thin sheets subjected to different loading conditions such as shear and corner loadings (Jenkins et al., 1998; Blandino et al., 2002; Wong and Pellegrino, 2006).

The remainder of this paper is organized as follows. Section 2 describes the experimental procedures and techniques used to generate and measure wrinkle profiles. Section 3 presents the experimental results. In Section 4, modeling and simulations of stretch-induced wrinkling with different material models are presented, emphasizing the effects of viscoelasticity. Section 5 discusses the comparison between experiments and modeling, followed by a brief summary in Section 6.

## 2. Experimental method

The material used in this study was a commercial grade polyethylene (Husky black plastic sheeting, manufactured by

<sup>\*</sup> Corresponding author. Tel.: +1 512 471 7558; fax: +1 512 471 5500.

E-mail address: [ruihuang@mail.utexas.edu](mailto:ruihuang@mail.utexas.edu) (R. Huang).

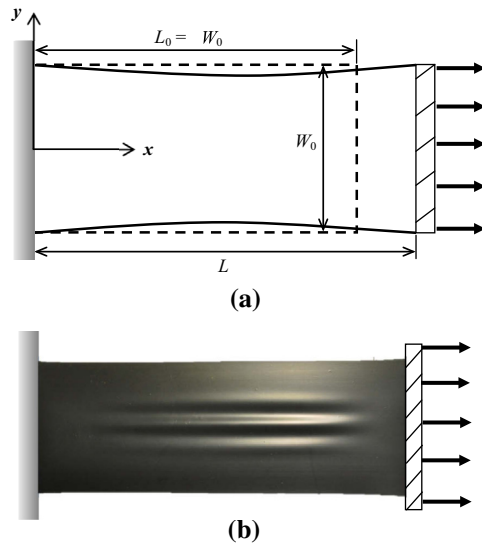


**Fig. 1.** (a) Schematic illustration of a rectangular sheet with two clamped-ends, subject to uniaxial stretch. (b) An optical image of a stretch-wrinkled polyethylene sheet ( $\varepsilon \sim 10\%$ ).

Poly-America) in the form of a thin sheet with nominal thickness,  $h_0 = 0.1$  mm. The first set of specimens had in-plane dimensions (after clamping) of:  $L_0 = 250$  mm and  $W_0 = 100$  mm, with the length-to-width aspect ratio  $\alpha = 2.5$  and the width-to-thickness ratio  $\beta = 1000$ . A second set of specimens was prepared with  $L_0 = 200$  mm and hence  $\alpha = 2$ . It was found that the as-received polyethylene sheet was not perfectly flat but had initial wrinkles and creases. In order to make the sheet flat, each specimen was first heat-treated by placing the sheet in between two plexiglas plates at a temperature of  $75^\circ\text{C}$  for 24 h, and then cooling slowly to room temperature. This process helped in removing the creases and attaining a flat sheet with negligible initial curvature.

Next, a speckle pattern was made on the surface of the specimen by using a white gel pen of 0.7 mm tip radius, covering the whole width of the specimen, with a height of approximately 15 mm in the middle of the specimen. This speckle pattern was used to determine the displacements and strains using the three-dimensional digital image correlation (3D-DIC) technique. The 3D-DIC technique is a combination of the stereo-vision technique and the digital image correlation (DIC) (Luo et al., 1993; Sutton et al., 2009). It relates the 3D geometry to a reference state (before deformation) so that the corresponding displacements and displacement gradients can be determined. Several references on applications of 3D-DIC in experimental mechanics can be found in Orteu (2009). This technique was used in the present study to measure three-dimensional geometry of the wrinkles in polyethylene sheets.

After forming the speckle pattern, the specimen was clamped at the two ends in a specially designed jig (Nayyar, 2013), which allowed proper alignment of the sheet with respect to the clamps. To hold the clamped specimen in the Instron tension test machine, a pinned support was used at each end so that the clamps were free to rotate with respect to the pin, minimizing the twisting moment due to any misalignment. After installing the clamped polyethylene sheet specimen onto the Instron machine, a small tensile strain ( $\leq 0.5\%$ ) was applied to reduce the initial undulations and slack in the sheet. The polyethylene sheet was then stretched up to 140% under displacement control at two different strain rates:  $0.0169\text{ s}^{-1}$  and  $0.00169\text{ s}^{-1}$ . The evolution of the wrinkle amplitude with time was recorded using the 3D-DIC system. Fig. 2 shows the experimental setup: two CCD cameras, each with

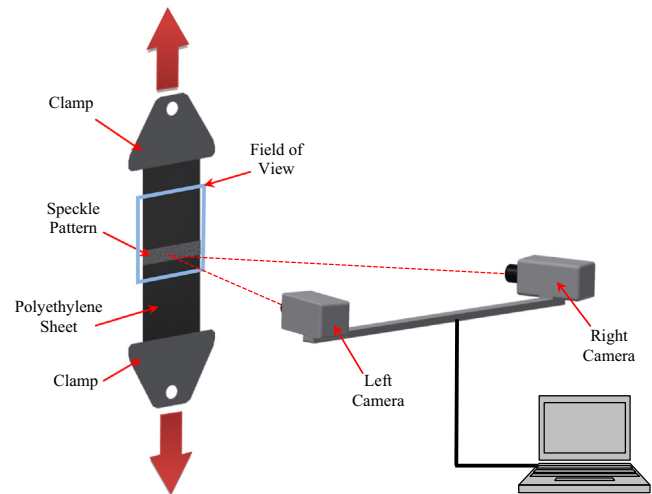


**Fig. 2.** Schematic illustration of the 3D-DIC setup used for stretching tests and wrinkle measurements with a clamped thin sheet.

a resolution of  $1624 \times 1236$  pixels were used to record the central portion of the specimen that was decorated with the speckle pattern. The two cameras were placed approximately at a distance of 1.3 m away from the specimen with a distance of 0.45 m from each other. This scheme along with a 50 mm lens resulted in a field of view of about  $100\text{ mm} \times 100\text{ mm}$ . The field of view of the two cameras was adjusted in such a way that the speckled region of the specimen was always visible as the sheet was stretched up to 140%. A commercial 3D-DIC software package, ARAMIS, was used to register the images from the two cameras and to calculate the displacement and strain field over the speckled region. Using this setup, the polyethylene sheet specimen was found to have a resolution of 9–10 pixels/mm, providing a displacement resolution of  $\sim 0.02$  mm. A total of 19 specimens were measured as summarized in Table 1.

### 3. Experimental results

Fig. 3 shows the optical images and the wrinkle profiles of a polyethylene sheet ( $\alpha = 2.5$ ) stretched to different nominal strain levels ( $\varepsilon = 0, 0.1, 0.2, 0.3$  and  $0.4$ ) at a strain rate of  $\dot{\varepsilon} = 0.00169\text{ s}^{-1}$ . Referring to Fig. 1, the nominal strain is defined as,  $\varepsilon = \delta/L_0$ , where  $\delta = L - L_0$  is the end displacement. The wrinkle profiles were obtained from the out-of-plane displacement,  $u_z(L/2, y)$ , measured by 3D-DIC along the line  $x = L/2$ . It should be noted that the sheet was not perfectly flat at zero strain even after the heat treatment. The observed initial undulations are partly due to small geometric misalignments at the clamped ends and partly due to gravity loading, which are eliminated once a small tensile strain is applied. Subsequently, stretch-induced wrinkles form near the center of the sheet, with a profile that appears

**Table 1**  
Summary of wrinkle measurements.

Aspect ratio $\alpha$	2.5	2.5	2	2
Strain rate ( $\text{s}^{-1}$ )	0.00169	0.0169	0.00169	0.0169
Number of specimens	5	7	3	4
Average peak amplitude (mm)	0.368	0.343	0.538	0.523
Standard deviation (mm)	0.045	0.039	0.027	0.082
Average strain at peak amplitude	0.111	0.109	0.100	0.088
Standard deviation	0.017	0.022	0.004	0.007
Average amplitude at 30% strain (mm)	0.166	0.133	0.245	0.112
Standard deviation (mm)	0.030	0.024	0.035	0.076

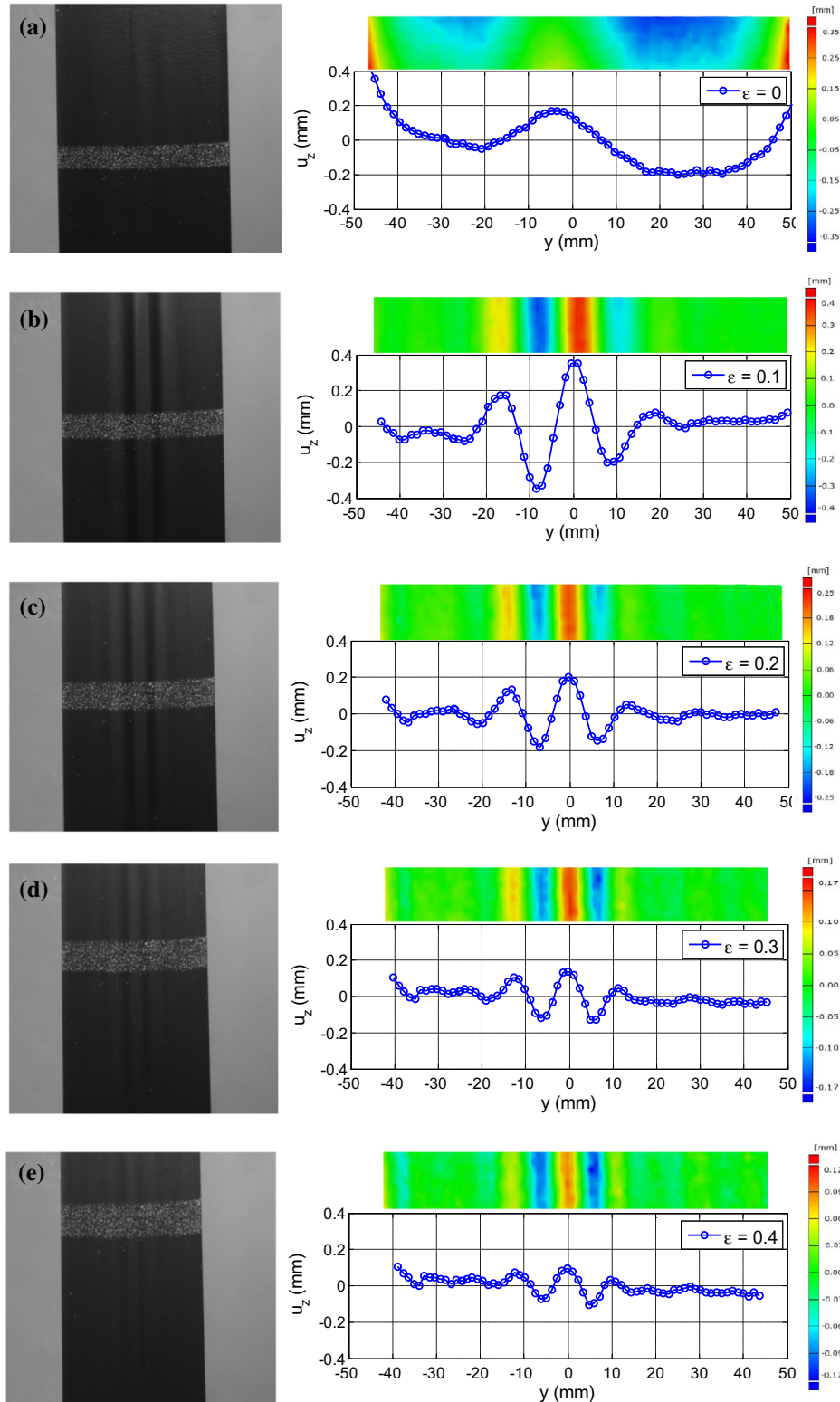


**Fig. 3.** Optical images and deflection profiles of stretch-induced wrinkles in a polyethylene sheet at different nominal strain levels. (a)–(e)  $\varepsilon = 0, 0.1, 0.2, 0.3$  and  $0.4$ . The strain rate  $\dot{\varepsilon} = 0.00169 \text{ s}^{-1}$ . The colored images are the out-of-plane displacement contours obtained from 3D-DIC for the marked region of the sheet.

to be largely independent of the initial undulations. Similar wrinkle profiles were obtained for two different strain rates ( $\dot{\varepsilon} = 0.0169 \text{ s}^{-1}$  and  $0.00169 \text{ s}^{-1}$ ) and two sets of specimens with different aspect ratios ( $\alpha = 2$  and  $2.5$ ). The wrinkle amplitude, defined as

$A = [\max\{u_z(L/2, y)\} - \min\{u_z(L/2, y)\}]/2$ , is plotted as a function of the nominal strain in Fig. 4. The post-buckling behavior of a hyper-elastic thin sheet was examined previously using finite element simulations (Nayyar et al., 2011); the corresponding simulation

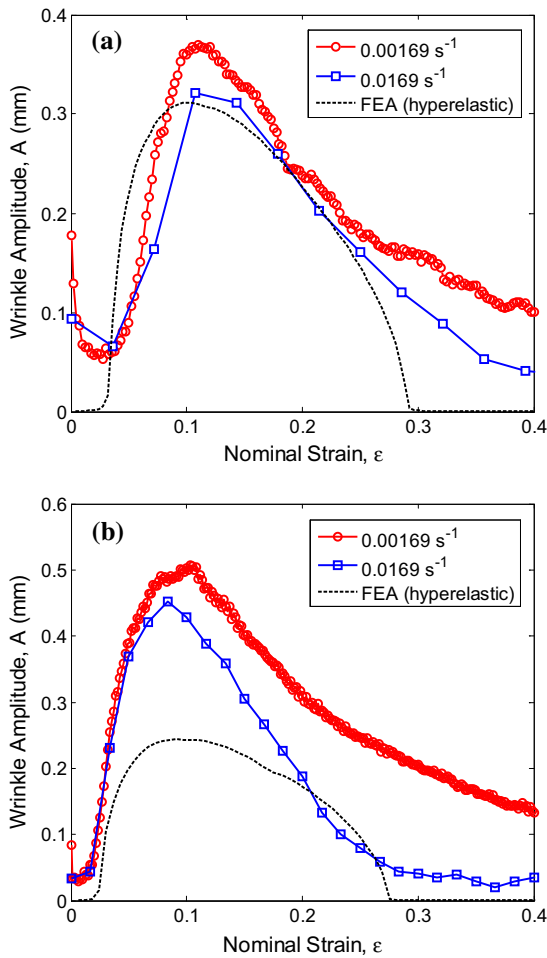


**Fig. 4.** Measured wrinkle amplitude as a function of nominal strain for polyethylene sheets, with  $\alpha = 2.5$  and  $2$ , respectively in (a) and (b), in comparison with finite element simulations of hyperelastic thin sheets.

results are also shown in Fig. 4 for comparison. The following important observations are noted:

- For both strain rates, the initial undulations with amplitudes in the range of 0.05–0.2 mm are removed rapidly upon application of a small tensile strain.
- After elimination of the initial undulations, wrinkle amplitude increases rapidly with the nominal strain. However, the presence of the initial undulations makes it difficult to accurately identify the critical strain for onset of stretch-induced wrinkling. Approximately, the critical strain may be estimated as the strain at which the wrinkle amplitude starts to increase; this is around 3–5% and compares well with the previous predictions by finite element analyses (Zheng, 2009; Nayyar et al., 2011).
- The amplitude continues to increase with strain and reaches a peak at around 10% strain. The peak amplitude of the wrinkles is weakly dependent on strain rate, but appears to depend strongly on the aspect ratio. For  $\alpha = 2.5$  the maximum amplitude is between 0.29 mm and 0.44 mm, while for  $\alpha = 2$  the maximum amplitude is between 0.45 mm and 0.65 mm. Table 1 lists the average and standard deviation from all measurements.
- Upon further increase in the nominal strain, the wrinkle amplitude begins to decrease steadily, and the wrinkle amplitude appears to depend on the strain rate.

Evidently, the experimental data for the wrinkle amplitude evolution are in qualitative agreement with the numerical simulations, but a few discrepancies are noticeable. First, the wrinkle amplitude at small strains ( $\epsilon \leq 0.03$ ) could not be predicted due to the initial undulations of the specimens; this also hinders the ability to identify the critical strain for the onset of wrinkling. Second, the numerical simulations underestimate the peak wrinkle amplitude, especially for  $\alpha = 2$ . Finally and most remarkably, unlike in the numerical simulations, the wrinkle amplitude does not go down to zero at large strains ( $\epsilon > 0.30$ ) in the experiments: while the numerical simulations predicted that the stretch-induced wrinkling is completely flattened beyond a moderately large strain ( $\epsilon > 0.30$ ) for a hyperelastic thin sheet, in the experiments the wrinkles remained observable up to  $\epsilon = 0.4$  (see Fig. 3). Furthermore, the residual wrinkle amplitude appears to be rate dependent. The differences between the experiments and the simulations indicate that the viscoelastic or viscoplastic response of polyethylene must play a crucial role in the wrinkling behavior.

In order to determine the constitutive model for polyethylene, we performed standard uniaxial tension tests using narrow strips of polyethylene with  $L_0 = 150$  mm,  $W_0 = 10$  mm, and  $h_0 = 0.1$  mm, for which wrinkling is not expected due to the relatively small width-to-thickness ratio ( $\beta = 100$ ). Fig. 5(a) shows the stress–strain curves measured at three different strain rates with a bilinear loading and unloading history. The stress–strain behavior exhibits characteristics of a nonlinear viscoelastic or viscoplastic material, with

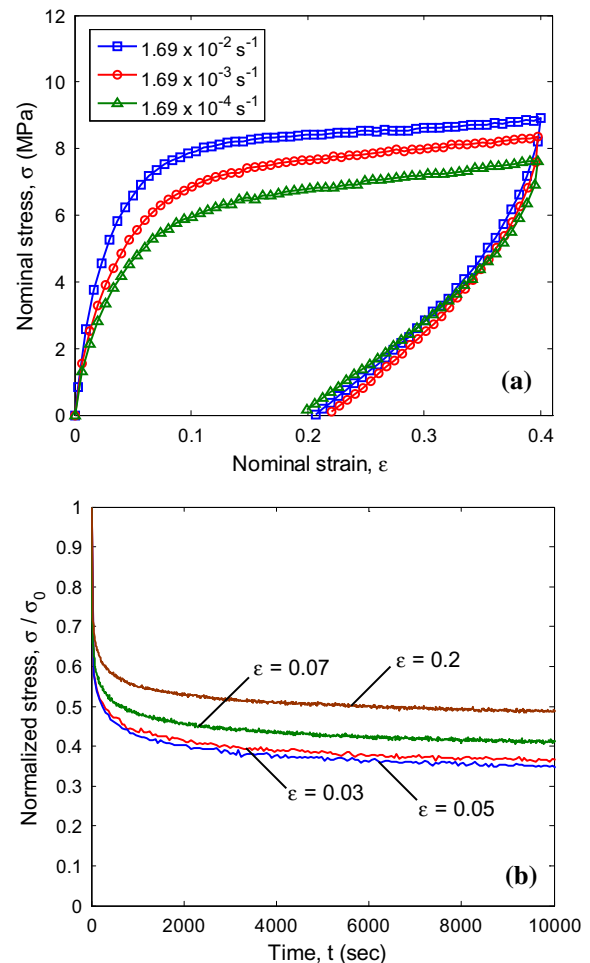


**Fig. 5.** (a) Nominal stress–strain diagrams under uniaxial tension tests at different strain rates, using narrow strips of polyethylene; (b) stress relaxation curves measured at different strain levels.



rate-dependence as well as a residual strain at the end of unloading. Additionally, the results of stress relaxation tests performed at different strain levels are shown in Fig. 5(b). Here, the polyethylene strip was first stretched at a strain rate of  $0.0169 \text{ s}^{-1}$  to the indicated strain level and then held constant while the time decay of the nominal stress was measured. The stress in Fig. 5(b) is normalized by the initial stress at the beginning of the relaxation test. The normalized stress relaxation curves are similar to typical viscoelastic relaxation of polymers, but they do not collapse onto a single curve, indicative of a nonlinear viscoelastic response.

#### 4. Modeling and simulations

While most previous studies on wrinkling of thin sheets have assumed the material to be elastic (Segedin et al., 1988; Friedl et al., 2000; Cerda et al., 2002; Zheng, 2009; Puntel et al., 2011; Nayyar et al., 2011; Healey et al., 2013), the results discussed in Section 3 clearly indicate that the viscoelastic nature of the polyethylene sheet influences the evolution of the wrinkling significantly. In this section, two different viscoelastic constitutive models – a hyper-viscoelastic (HVE) model and a parallel network (PN) model – are calibrated to the data on polyethylene over the range of strain rates and time scales considered. Then the evolution of the stretch-induced wrinkling is examined through numerical simulations with both models. It is found that the PN model is better suited to capture both the constitutive and wrinkling behaviors of the polyethylene thin sheets. While other constitutive models may be considered to further refine the modeling and simulations, the HVE and PN models have been implemented in ABAQUS and are used in the present study to represent two types of viscoelastic models.

##### 4.1. Constitutive modeling

The hyper-viscoelasticity (HVE) model is a time-domain generalization of the hyperelastic constitutive model for finite-strain viscoelasticity (Simo, 1987; ABAQUS, 2012). It is also a generalized

Maxwell model that incorporates nonlinear geometry associated with large deformation. As illustrated in Fig. 6(a), a HVE model can be represented by a mechanical analog with an elastic branch and any number of viscoelastic branches in parallel. This generalization yields a constitutively linear viscoelastic behavior in the sense that the dimensionless stress relaxation function is independent of the magnitude of the deformation. On the other hand, the nonlinear PN model, as illustrated in Fig. 6(b), consists of two branches representing two parallel networks of the polymer: network 'A' is hyperelastic and network 'B' is nonlinear viscoelastic, where an intrinsically nonlinear viscoelastic behavior is constitutively described by a rate equation. More than one nonlinear viscoelastic network may be used if necessary (Bergström and Boyce, 1998; ABAQUS, 2012).

In the present study, the incompressible neo-Hookean model is used for the hyperelastic instantaneous stress in both models. Under uniaxial tension, the instantaneous Cauchy stress is

$$\sigma_0 = \mu_0 \left( \lambda^2 - \frac{1}{\lambda} \right) \quad (1)$$

where  $\mu_0$  is the instantaneous shear modulus and  $\lambda = 1 + \varepsilon$  is the axial stretch corresponding to the nominal strain  $\varepsilon$ . In the HVE model, a time-dependent shear relaxation modulus,  $\mu(t)$ , is assumed to take the form of a Prony series,

$$\mu(t) = \mu_0 \left[ 1 - \sum_{i=1}^N g_i (1 - e^{-t/\tau_i}) \right] \quad (2)$$

where the parameters  $\mu_0$ ,  $g_i$  and  $\tau_i$  ( $i = 1, 2, \dots, N$ ) are to be determined experimentally.

It is found that, with a single viscoelastic branch in Fig. 6(a), the HVE model can be used to fit the uniaxial stress–strain response of polyethylene for each strain rate (but not for unloading), as shown in Fig. 7(a). Table 2 lists the material parameters obtained by fitting, where the instantaneous shear modulus ( $\mu_0$ ) and the long-term shear modulus,  $\mu_\infty = \mu_0(1 - g_1)$  are kept constant for the three different strain rates, but the time scale  $\tau$  is varied to fit the uniaxial stress–strain data at each strain rate. As the strain rate increases, the associated time scale decreases and the stress increases. Therefore, the HVE model may be used to simulate the stress–strain behavior of polyethylene at a particular strain rate, but the strain rate dependence has to be accounted for by varying the viscoelastic time scale.

We note that the stress relaxation behavior observed in Fig. 5(b) cannot be captured by the HVE model with a single viscoelastic branch. While it is possible to fit the relaxation response by using more than one viscoelastic branch (hence more than one time scale) in the HVE model, it requires a different set of parameters for each relaxation curve. In general, it is unlikely that the relaxation curves of polyethylene at different strain levels could be fitted by using the HVE model with a single set of parameters in the Prony series, due to the intrinsically nonlinear viscoelastic behavior of the material. For the same reason, the rate-dependent stress–strain behavior of polyethylene (Fig. 5(a)) cannot be captured by the HVE model using multiple branches with a single set of parameters. Approximately, for a specific strain rate, the stress–strain behavior under monotonic loading (without unloading) may be simulated by using a single time scale in the HVE model (see Fig. 7(a)).

Next, for the nonlinear PN model, the total Cauchy stress under uniaxial tension is

$$\sigma = \mu_A \left( \lambda_A^2 - \frac{1}{\lambda_A} \right) + \mu_B \left( (\lambda_B^e)^2 - \frac{1}{\lambda_B^e} \right) \quad (3)$$

where  $\lambda_A = \lambda$ ,  $\lambda_B^e = \lambda / \lambda_B^\sigma$ , and  $\mu_A$  and  $\mu_B$  are the elastic shear modulus of networks A and B, respectively. While the network A is hyperelastic,

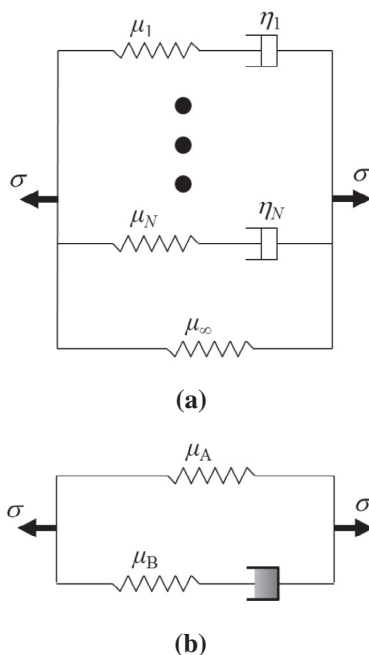
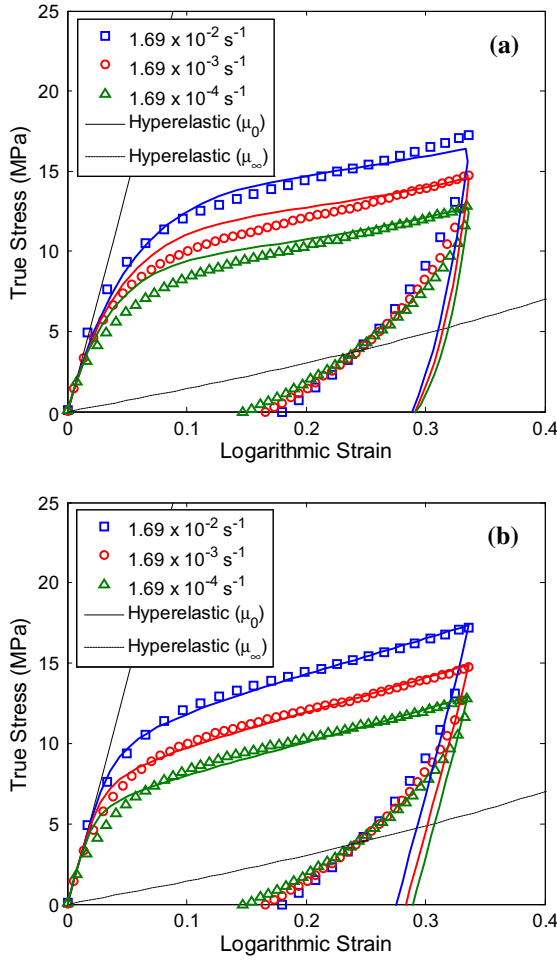


Fig. 6. Two viscoelastic models represented by mechanical analogs: (a) a hyper-viscoelastic model; (b) a parallel network nonlinear viscoelastic model.



**Fig. 7.** Fitting of the uniaxial stress–strain diagrams of polyethylene measured at different strain rates using the HVE model (a) and the parallel network model (b), with the parameters listed in Tables 1 and 2, respectively. The lines represent the simulated results in comparison with the experimental data represented by the symbols.

**Table 2**

Parameters used to fit the uniaxial stress–strain response of polyethylene at different strain rates with a single viscoelastic branch in the HVE model.

Strain rate $\dot{\varepsilon}$ ( $s^{-1}$ )	Shear moduli		Relaxation time scale $\tau$ (s)	Normalized strain rate $\dot{\varepsilon}\tau$
	$\mu_0$ (MPa)	$\mu_\infty$ (MPa)		
$1.69 \times 10^{-4}$	90	4.5	200	0.0338
$1.69 \times 10^{-3}$	90	4.5	25	0.0423
$1.69 \times 10^{-2}$	90	4.5	3	0.0507

the viscoelastic deformation in the network  $B$  is modeled by the multiplicative decomposition of the total deformation into elastic and viscous parts. A nonlinear flow rule is used to describe the viscous deformation of the network  $B$ . By a power-law strain hardening model, the equivalent creep strain rate  $\dot{\varepsilon}^{cr}$  is

$$\dot{\varepsilon}^{cr} = (Bq_B^n[(m+1)\bar{\varepsilon}^{cr}]^m)^{\frac{1}{m+1}} \quad (4)$$

where  $\bar{\varepsilon}^{cr}$  is the equivalent creep strain,  $q_B$  is the equivalent deviatoric Cauchy stress, and  $B$ ,  $m$  and  $n$  are the material parameters ( $-1 < m \leq 0$  and  $B, n > 0$ ). For the case of uniaxial tension, the flow rule can be reduced to a scalar form:

$$\frac{\dot{\lambda}_B^{cr}}{\lambda_B^{cr}} = \dot{\varepsilon}^{cr} = (B\sigma_B^n[(m+1)\bar{\varepsilon}^{cr}]^m)^{\frac{1}{m+1}} \quad (5)$$

By integrating the first part of Eq. (5), we obtain the equivalent creep strain in terms of the axial stretch:  $\bar{\varepsilon}^{cr} = \ln(\lambda_B^{cr})$ . The rate equation can then be re-written as

$$\dot{\lambda}_B^{cr} = \lambda_B^{cr} \left( B\sigma_B^n[(m+1)\ln(\lambda_B^{cr})]^m \right)^{\frac{1}{m+1}} = \bar{B}\lambda_B^{cr} [\ln(\lambda_B^{cr})]^{\frac{m}{m+1}} \left( \frac{\sigma_B}{\mu_B} \right)^{\frac{n}{m+1}} \quad (6)$$

where  $\sigma_B = \mu_B \left[ \left( \frac{\lambda}{\lambda_B^{cr}} \right)^2 - \frac{\lambda_B^{cr}}{\lambda} \right]$  and  $\bar{B} = (B\mu_B^n(m+1)^m)^{\frac{1}{m+1}}$ . Thus, by integrating Eq. (6),  $\lambda_B^{cr}$  can be obtained as a function of time, with the initial condition,  $\lambda_B^{cr} = 1$  at  $t = 0$ . The total stress is then obtained as a function of time for the case of uniaxial tension from Eq. (3).

Consider two limiting cases using the PN model. First, when the applied strain rate  $\dot{\lambda} \rightarrow \infty$ , the creep strain approaches zero ( $\lambda_B^{cr} \rightarrow 1$ ), and Eq. (3) becomes

$$\sigma = (\mu_A + \mu_B) \left( \lambda^2 - \frac{1}{\lambda} \right) \quad (7)$$

which corresponds to the elastic limit with the instantaneous shear modulus  $\mu_0 = (\mu_A + \mu_B)$ . Second, when the strain rate  $\dot{\lambda} \rightarrow 0$ , the creep strain in network  $B$  approaches the total strain,  $\lambda_B^{cr} \rightarrow \lambda$ , and Eq. (3) becomes

$$\sigma = \mu_A \left( \lambda^2 - \frac{1}{\lambda} \right) \quad (8)$$

which corresponds to the long term elastic limit ( $\mu_\infty = \mu_A$ ). For a uniaxial tension test with a finite strain rate, the viscoelastic stress–strain behavior by the PN model is bounded by these two elastic limits.

In order to determine the material parameters in the PN model ( $\mu_A$ ,  $\mu_B$ ,  $B$ ,  $m$  and  $n$ ), the stress–strain curves of polyethylene measured by the uniaxial tension tests (Fig. 5(a)) are used. First, the instantaneous elastic modulus of the PN model can be obtained by measuring the slope of the stress–strain curves at the early stage. As shown in Fig. 7(b), the initial slope ( $\varepsilon \rightarrow 0$ ) of the stress–strain curve yields the instantaneous modulus,  $\mu_0 = (\mu_A + \mu_B) = 90$  MPa. Next, we estimate the long-term elastic modulus by the slope at relative large strains ( $\varepsilon > 0.2$ ), which yields  $\mu_A = 4.5$  MPa. Note that both the instantaneous and long-term elastic moduli are the same as those in Table 2 for the HVE model. The other parameters in the PN model are associated with the nonlinear viscoelastic response and are determined by fitting the numerical simulations with the experimental measurements. A three-dimensional (3D) finite element model in ABAQUS is used with PN constitutive model to simulate the stress–strain response. By an iterative approach, the viscoelastic parameters listed in Table 3 are obtained as the best fit parameters. A comparison of the predicted response to the observed data is shown in Fig. 7(b). It is noted that, while the PN model predicts the constant strain-rate loading response quite well, the prediction for the unloading response is nearly linear and differs significantly from the experimental measurements.

To simulate the stress relaxation response (Fig. 5(b)), a 3D finite element model is employed including both the initial stretching and subsequent holding stages. Fig. 8 shows the simulated relaxation responses, in comparison with the relaxation tests at different strain levels. Using the parameters in Table 3 for the PN model, the simulated stress relaxation curves are in reasonable agreement with the experimental measurements. Therefore, the viscoelastic behavior of polyethylene under both the constant strain rate and stress relaxation conditions can be simulated using the PN model with the same set of material parameters. In other words, the nonlinear viscoelastic behavior of polyethylene can be captured reasonably well by the PN model, with the exception of the unloading behavior. For the present study on stretch-induced wrinkling, the effect of unloading is considered to be negligible.

**Table 3**

Material parameters used to fit the uniaxial tension stress–strain response of polyethylene with the PN model.

$\mu_A$	4.5 MPa
$\mu_B$	85.5 MPa
$B$	$1.3 \times 10^{-7} \text{ MPa}^{-n} \text{ s}^{-(m+1)}$
$n$	5.12
$m$	−0.465

#### 4.2. Dimensional analysis of wrinkling

Before embarking on numerical simulations of stretch-induced wrinkling with the viscoelastic models, we explore the problem through dimensional analysis. The boundary-value problem (BVP) as sketched in Fig. 1(a) contains a single loading parameter,  $\delta$ , the end displacement, which is normalized by the length of the sheet to define the nominal strain,  $\varepsilon = \delta/L_0$ . The dimensions of the sheet are parameterized by two dimensionless ratios,  $\alpha = L_0/W_0$  and  $\beta = W_0/h_0$ . The remaining physical parameters of the BVP depend on the constitutive model for the material. Regardless of the material model, the wrinkle amplitude normalized by the sheet thickness is a dimensionless quantity and can only be a function of the dimensionless parameters of the BVP. In general, we may write

$$A/h_0 = f(\varepsilon, \alpha, \beta; M_i, i = 1, 2, 3, \dots) \quad (9)$$

where  $M_i (i = 1, 2, 3, \dots)$  represent a set of dimensionless parameters related to the material model. The dimensional consideration dictates that the wrinkle amplitude as a function of the applied strain does not depend on the elastic stiffness of the material alone. In the case of a linear elastic material, it depends on Poisson's ratio,

but not Young's modulus. In the case of an elastic–plastic material, it depends on the yield stress and hardening modulus, both normalized by the elastic modulus. If the material behavior is time dependent, the time or the loading rate can be normalized by the material time scales in the constitutive model so that the wrinkle amplitude becomes rate/time-dependent. A few specific material models are considered as follows.

##### 4.2.1. Elastic materials

First, if the material is isotropic and linear elastic, the only dimensionless parameter in the material model is Poisson's ratio, and thus

$$A/h_0 = f_E(\varepsilon, \alpha, \beta; \nu) \quad (10)$$

If the material is isotropic and hyperelastic, described by the incompressible neo-Hookean model, the Poisson's ratio is invariably 0.5, and the material model does not have any other dimensionless parameter. Therefore,

$$A/h_0 = f_E^*(\varepsilon, \alpha, \beta) \quad (11)$$

This is the case considered in the previous study (Nayyar et al., 2011).

##### 4.2.2. Hyper-viscoelastic materials

Next, for the HVE model as described in Section 4.1, we have a set of time scales  $\tau_i (i = 1, 2, \dots, N)$  and a set of dimensionless parameters,  $g_i (i = 1, 2, \dots, N)$ . Therefore, the wrinkle amplitude under a ramp loading with a constant strain rate ( $\dot{\varepsilon}$ ) takes the form

$$A/h_0 = f_{HVE}(\varepsilon, \alpha, \beta, \dot{\varepsilon}\tau_i, g_i; i = 1, \dots, N) \quad (12)$$

It is expected that the time-dependent material behavior renders a history-dependent wrinkling behavior. For example, in the case of a

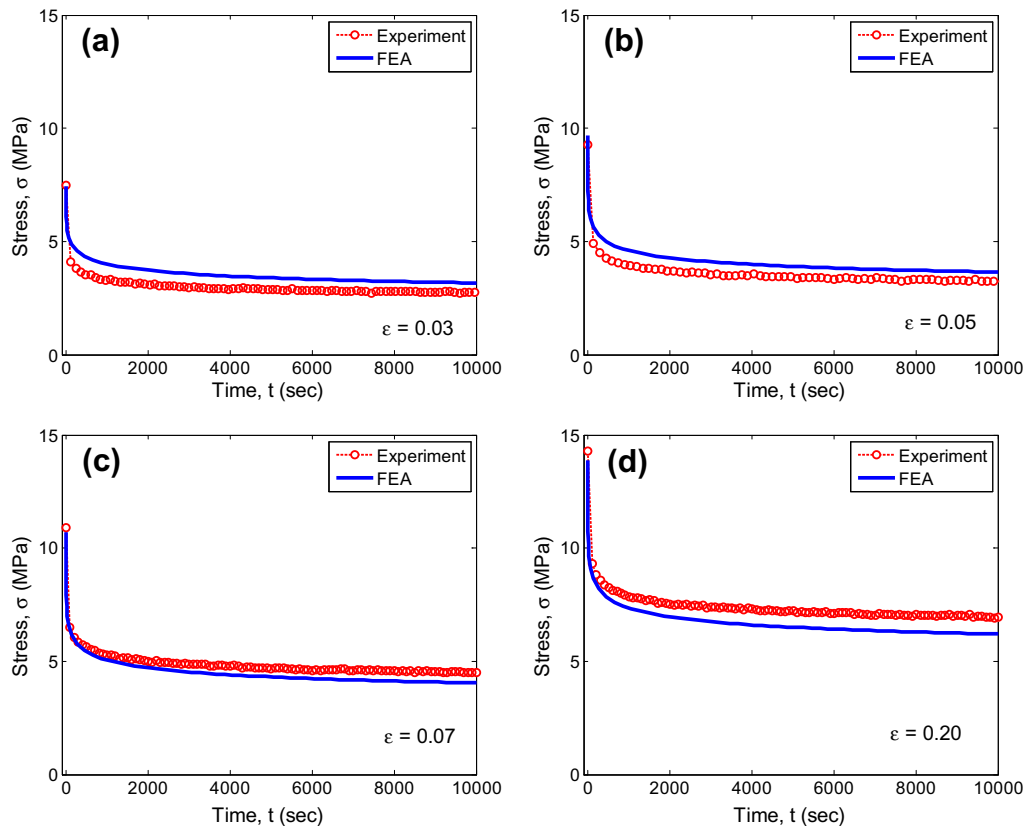


**Fig. 8.** Comparison between measured uniaxial stress relaxation of polyethylene and numerical simulations using the parallel network model at different strain levels. (a)–(d) For  $\varepsilon = 0.03, 0.05, 0.07$  and  $0.20$ .

relaxation test (Nayyar, 2013), the wrinkle amplitude is a function of time ( $t$ ), which can be written as

$$A(t)/h_0 = f_{\text{HVE}}^r(\varepsilon, \alpha, \beta, t/\tau_i, g_i; i = 1, \dots, N) \quad (13)$$

At the long-time limit ( $t \rightarrow \infty$ ), it is expected that the wrinkle amplitude in the HVE model approaches that in the hyperelastic model, namely

$$\lim_{t \rightarrow \infty} A(t)/h_0 = f_E^*(\varepsilon, \alpha, \beta) \quad (14)$$

In particular, for a two-branch HVE model ( $N = 1$ ), the wrinkle amplitude may be written as

$$A/h_0 = f_{\text{HVE}}(\varepsilon, \alpha, \beta, \dot{\varepsilon}\tau, \mu_\infty/\mu_0) \quad (15)$$

In comparison with Eq. (11) for the hyperelastic sheets, the normalized wrinkle amplitude depends on the viscoelastic parameters of the HVE model in addition to the nominal strain and aspect ratios. The strain-rate dependence results naturally from the viscoelastic time scale. Moreover, the wrinkle amplitude depends on the ratio between the two elastic moduli,  $\mu_\infty/\mu_0$ . These effects are examined through numerical simulations in Section 4.3.

#### 4.2.3. Nonlinear viscoelastic materials

Many forms of nonlinear viscoelastic constitutive models have been developed to describe time/rate-dependent, large deformation behavior of polymers (e.g., Bergström and Boyce, 1998; Boyce et al., 2000; Drozdov and Gupta, 2003; Shim et al., 2004; Dusunceli and Colak, 2006; Ayoub et al., 2010). For the PN model as discussed in Section 4.1, the material parameters include  $B, m, n$ , and two shear moduli,  $\mu_A$  and  $\mu_B$ . The normalized wrinkle amplitude can be written as a function of seven dimensionless quantities:

$$A/h_0 = f_{\text{PN}}(\varepsilon, \alpha, \beta, \bar{\tau}\dot{\varepsilon}, \mu_A/\mu_B, n, m) \quad (16)$$

where  $\bar{\tau} = (B\mu_B^m)^{-1/(m+1)}$  is a time scale. Using the material parameters listed in Table 3, the time scale  $\bar{\tau} = 2.4 \times 10^{-6}$  s. However, as suggested by Eq. (6), the relaxation time scale in the nonlinear viscoelastic model depends on the stress  $\sigma_B$ , which could vary both in time and in space. Nevertheless, with the presence of the time scale  $\bar{\tau}$  in the model, strain rate dependence of the wrinkling behavior is expected. In addition, the normalized wrinkle amplitude depends

on the two dimensionless parameters in the PN model,  $n$  and  $m$ . Similar to the HVE model, the wrinkle amplitude also depends on the modulus ratio,  $\mu_A/\mu_B$ , in the PN model.

In addition to the wrinkle amplitude, the other quantities may be analyzed similarly by the dimensional consideration. For example, the wrinkle wavelength normalized by the sheet thickness,  $\lambda/h_0$ , should in general depend on the same set of dimensionless parameters as the wrinkle amplitude for each material model, as discussed further in Section 5. Moreover, the critical condition, in terms of either the applied strain ( $\varepsilon_c$ ) or the applied force ( $P_c$ ), can be expressed in similar forms:

$$\varepsilon_c = \varepsilon_c(\alpha, \beta; M_i, i = 1, 2, 3 \dots) \quad (17)$$

or

$$\frac{P_c}{EW_0 h_0} = f_c(\alpha, \beta; M_i, i = 1, 2, 3 \dots) \quad (18)$$

where  $E$  can be one of the material parameters with the dimension of elastic modulus. The critical conditions for stretch-induced wrinkling have been studied previously for linear elastic thin sheets (Puntel et al., 2011; Healey et al., 2013) and hyperelastic sheets (Zheng, 2009; Nayyar et al., 2011; Nayyar, 2013).

#### 4.3. Finite element simulations

Previous studies have shown that, for an elastic thin sheet subject to uniaxial stretch with clamped ends, compressive stresses develop in the transverse direction due to Poisson's effect and the specific boundary conditions (Friedl et al., 2000; Nayyar et al., 2011). The critical condition for onset of stretch-induced wrinkling depends on both the magnitude and the distribution of the compressive stress. With non-uniform stress distribution in the sheet, the effect of viscoelasticity on the development of compressive stresses is nontrivial. A two-dimensional (2D) finite element analysis is performed using the HVE material model and a quasi-static loading procedure in ABAQUS/Standard, where the sheet is modeled by quadrilateral plane-stress elements (CPS4R) assuming no wrinkles. Fig. 9(a) shows the distribution of transverse compressive stress ( $\sigma_y$ ) at nominal strain  $\varepsilon = 0.1$  for a rectangular sheet with the

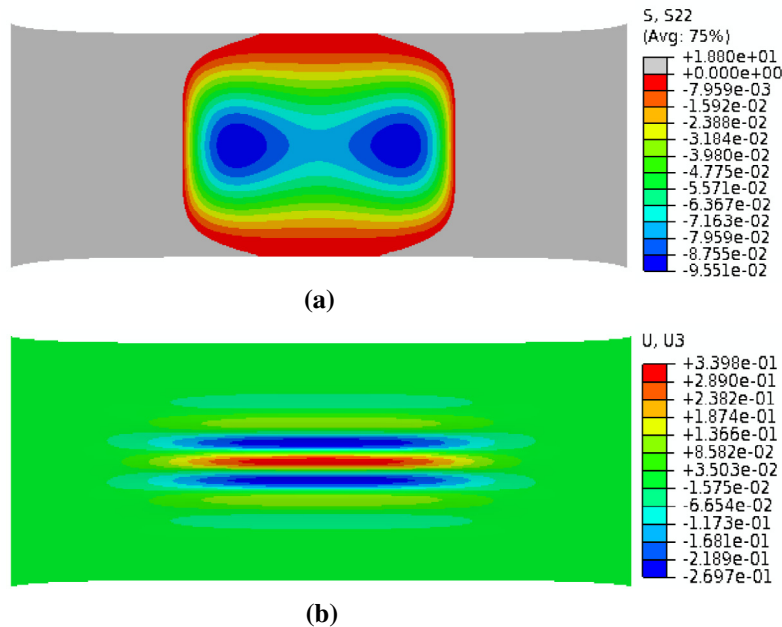


**Fig. 9.** (a) Distribution of compressive transverse stress by 2D finite element analysis; (b) stretch-induced wrinkles by post-buckling analysis. Both are for a hyper-viscoelastic thin sheet stretched at 10% nominal strain with a strain rate of  $0.00169 \text{ s}^{-1}$ .



length-to-width ratio  $\alpha = 2.5$ . The overall stress distribution pattern is similar to that for a hyperelastic sheet in the previous study (Nayyar et al., 2011). However, the stress magnitude is rate dependent for the hyper-viscoelastic sheet. As shown in Fig. 10(a), the maximum compressive stress in the sheet is plotted as a function of the nominal strain for different strain rates. The time scales in Table 2 are used for the three strain rates. For comparison, the maximum compressive stresses are plotted for two hyperelastic sheets with the initial shear modulus equal to the instantaneous and equilibrium moduli,  $\mu_0$  and  $\mu_\infty$ , respectively. Apparently, the stress magnitude increases with the shear modulus for the hyperelastic sheet. However, the strain at which the compressive stress vanishes is independent of the shear modulus (Nayyar et al., 2011). For the hyper-viscoelastic sheet, while the overall stress behavior is similar, the stress magnitude increases with increasing strain rate, bounded by the two hyperelastic limits.

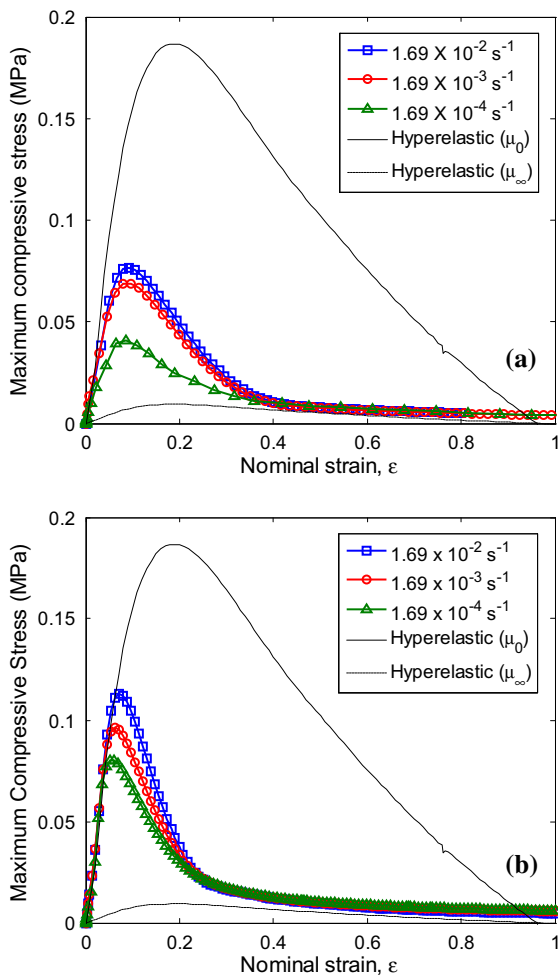
In order to perform the stress analysis of an end-clamped sheet using the PN nonlinear viscoelastic material model, a 3D finite element model is required in ABAQUS. The dimensions of the sheet are same as the polyethylene sheet used in the experiments:  $L_0 = 250$  mm,  $W_0 = 100$  mm, and  $h_0 = 0.1$  mm. For computational efficiency, a quarter model is used with one layer of C3D8R elements and the material is assumed to be nearly incompressible (with a bulk modulus  $K = 20$  GPa and  $K/\mu_0 \approx 200$ ). Each element has in-plane dimension of  $1 \text{ mm} \times 1 \text{ mm}$  and thickness of

0.1 mm. The mesh used here is first checked by using hyperelastic material properties in comparison with the results from the 2D plane-stress model. With the PN nonlinear viscoelastic model, the stress distribution is found to be qualitatively similar to those for both hyperelastic and hyper-viscoelastic sheets and is therefore not shown. The magnitude of the maximum compressive stress changes non-monotonically with the nominal strain (Fig. 10(b)). Similar to the HVE model, the stress magnitude increases with increasing strain rate, and it is bounded by the two hyperelastic limits corresponding to the instantaneous and equilibrium shear moduli,  $\mu_0$  and  $\mu_\infty$ , respectively. Unlike the HVE model, the rate dependence in the PN model is predicted by using a single set of material parameters as listed in Table 3 for the PN model. The stress magnitude by the PN model is slightly higher than by the HVE model. In both viscoelastic models, we note that the maximum compressive stress first follows the hyperelastic limit with the instantaneous shear modulus ( $\mu_0$ ) at relatively small strain levels and then approaches the hyperelastic limit with the equilibrium shear modulus ( $\mu_\infty$ ) at larger strain. The effect of viscoelasticity is thus most significant for intermediate strain levels (roughly, 0.05–0.3).

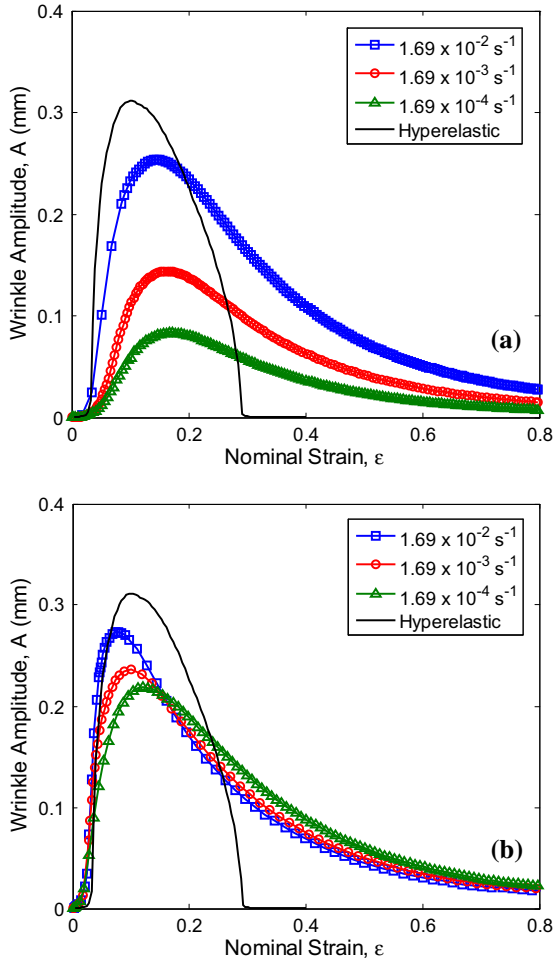
Next, to simulate stretch-induced wrinkling in the viscoelastic thin sheets, we perform buckling and post-buckling analyses using the HVE and PN material models in ABAQUS. Similar to the previous study for hyperelastic thin sheets (Nayyar et al., 2011), an eigenvalue buckling analysis is conducted first to obtain relevant eigenmodes; these modes are then used as the initial imperfections for the quasi-static post-buckling analysis. The shell elements (S4R) are used for hyper-viscoelastic sheets, while three-dimensional solid elements (C3D20R) are used for PN nonlinear viscoelastic sheets. Fig. 9(b) shows the simulated wrinkle pattern for a hyper-viscoelastic sheet stretched to a nominal strain of  $\varepsilon = 0.1$  at the strain rate  $1.69 \times 10^{-3} \text{ s}^{-1}$ ; using the PN model yields a similar wrinkle pattern. The wrinkle pattern is similar to the experimental wrinkle pattern in Fig. 1(b), as well as the pattern in a hyperelastic sheet shown in the previous study (Nayyar et al., 2011).

Fig. 11(a) shows the wrinkle amplitude as a function of the nominal strain for the hyper-viscoelastic sheet stretched at different strain rates along with a comparison to the results for a hyperelastic sheet. Recall that the wrinkle amplitude for a hyperelastic sheet is independent of its shear modulus (Nayyar et al., 2011). For the HVE model, the wrinkle amplitude depends on the viscoelastic time scale and increases with increasing strain rate (correspondingly, decreasing time scale), consistent with the increasing compressive stress shown in Fig. 10(a). As predicted by the dimensional analysis in Section 4.2, the normalized wrinkle amplitude depends on the dimensionless group,  $\dot{\varepsilon}\tau$ . As listed in Table 2, when the strain rate increases, the time scale  $\tau$  decreases but  $\dot{\varepsilon}\tau$  increases. Hence, the results in Fig. 11(a) indicate that the wrinkle amplitude increases with increasing  $\dot{\varepsilon}\tau$ . Theoretically it may be expected that the wrinkling behavior in a hyper-viscoelastic sheet approaches the same hyperelastic limit at both low and high strain rates. However, for the three strain rates considered in the present study, we only see that the wrinkle amplitude approaches the hyperelastic case when strain rate increases. More interestingly, while the wrinkle amplitude was predicted to vanish in the hyperelastic sheet beyond about 30% strain (Nayyar et al., 2011), the wrinkle amplitude in the hyper-viscoelastic sheet remains non-zero up to a much larger strain. This behavior agrees qualitatively well with the experimental results for the polyethylene sheet (Fig. 4).

The post-buckling analyses of nonlinear viscoelastic sheets by the PN model show qualitatively similar results as for the HVE model. As shown in Fig. 11(b), the wrinkle amplitude depends on the strain rate, but the rate dependence is not as strong as for the HVE model in Fig. 11(a). Here the rate dependence is predicted by the PN model using the single set of material parameters (Table 3). As



**Fig. 10.** Maximum compressive stress in a viscoelastic thin sheet ( $\alpha = 2.5$  and  $\beta = 1000$ ) subject to uniaxial stretch with three different strain rates, by numerical simulations using (a) HVE and (b) PN models, in comparison with two hyperelastic limits.



**Fig. 11.** Wrinkle amplitude in a viscoelastic thin sheet ( $\alpha = 2.5$  and  $\beta = 1000$ ) subject to uniaxial stretch with three different strain rates, by post-buckling simulations using (a) HVE and (b) PN models, in comparison with the hyperelastic limit.

indicated in Eq. (16), the normalized wrinkle amplitude depends on  $\bar{\tau}\dot{\epsilon}$ , where the time scale  $\bar{\tau}$  is a constant for the PN model used in the present study. Similar to the HVE model, the PN model predicts non-zero wrinkle amplitude well beyond  $\epsilon = 0.3$ , in contrast to the hyperelastic model.

For both the HVE and PN models, the wrinkle amplitude also depends on the modulus ratio,  $\mu_\infty/\mu_0$  or  $\mu_A/\mu_B$ , as indicated by the dimensional analysis in Section 4.2. Fig. 12 shows the numerical results corresponding to a fixed strain rate of  $0.0169 \text{ s}^{-1}$ . For the HVE model, we vary  $g_1$  or  $\mu_\infty$  while keeping  $\mu_0$  and  $\tau$  constant. As a result, the stiffness of the viscoelastic branch ( $\mu_1 = \mu_0 - \mu_\infty$ ) decreases with increasing ratio  $\mu_\infty/\mu_0$ . In this case, the viscoelastic effect lowers the wrinkle amplitude in the early stage but delays the suppression of wrinkling in the late stage. As the modulus ratio  $\mu_\infty/\mu_0$  increases, the wrinkling behavior approaches the hyperelastic behavior. Similarly, for the PN model, we vary the equilibrium shear modulus ( $\mu_\infty = \mu_A$ ) while keeping the instantaneous modulus ( $\mu_0 = \mu_A + \mu_B$ ) and other parameters ( $B$ ,  $m$ , and  $n$ ) constant. The wrinkle amplitude in this case follows the hyperelastic model in the early stage before reaching a peak amplitude. The peak amplitude depends on the modulus ratio and surprisingly exceeds the hyperelastic peak for  $\mu_\infty/\mu_0 = 0.25$  and  $0.45$ . The reason for the higher wrinkle amplitude is unclear. Apparently, the dependence of the wrinkling behavior on the modulus ratio is complicated by the nonlinear viscoelastic process in the PN model, and no clear trend can be observed from the numerical simulations.

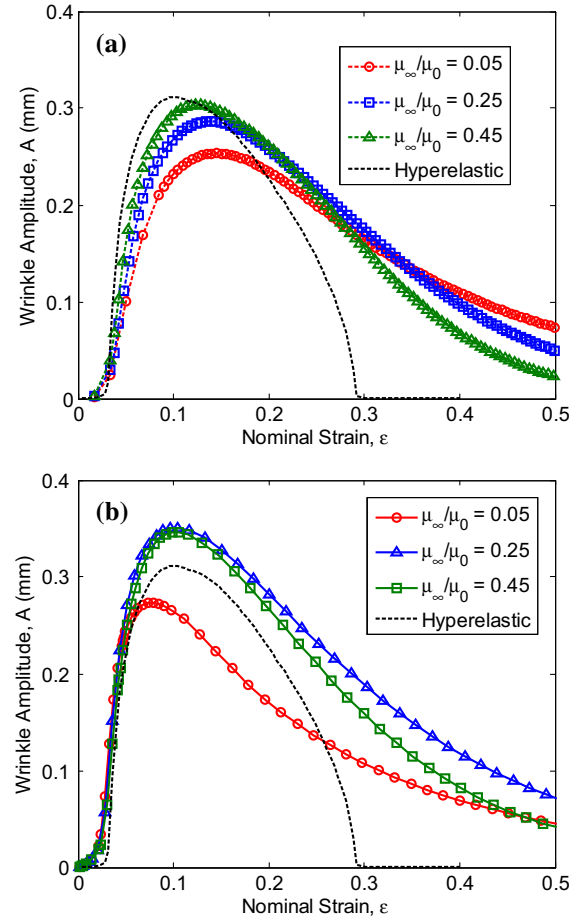


**Fig. 12.** Effect of modulus ratio ( $\mu_\infty/\mu_0$ ) on stretch-induced wrinkle amplitude in a viscoelastic thin sheet ( $\alpha = 2.5$  and  $\beta = 1000$ ), by numerical simulations using (a) HVE and (b) PN models.

## 5. Comparison and discussion

In this section, we present a direct comparison between the experimental measurements and numerical simulations. As shown in Fig. 13, the wrinkle profiles measured by 3D-DIC at different strain levels (with a strain rate of  $0.0169 \text{ s}^{-1}$  and  $\alpha = 2.5$ ) are compared to the simulated profiles using the PN nonlinear viscoelastic material model. Except for the initial undulation in the experiment, the number of wrinkles and the wrinkle amplitude predicted by the numerical simulation are in good agreement with the measurements. Fig. 14 compares the wrinkle amplitude for two different aspect ratios,  $\alpha = 2.5$  and  $2$ , each with two different strain rates as shown before in Fig. 4. The nonlinear PN model shows considerable improvement over the hyperelastic model (Fig. 4) in the overall agreement with the experiments. In particular, the viscoelastic model correctly predicts observable wrinkle amplitude well beyond  $\epsilon = 0.3$ . The maximum wrinkle amplitudes are under-predicted by the simulations, possibly due to the presence of initial undulations in the experiments. Although not shown here, the HVE model yields qualitatively similar wrinkling behavior, but with significantly lower wrinkle amplitude for  $\alpha = 2$  (Nayyar, 2013).

In the previous study on hyperelastic thin sheets (Nayyar et al., 2011), it was found that the wrinkle wavelength agrees closely with a scaling analysis by Cerda and Mahadevan (2003) despite their assumption of linear elasticity. They predicted that the wrinkle wavelength depends on the nominal strain and the sheet dimensions as  $\lambda \sim (Lh)^{1/2} \epsilon^{-1/4}$ , or in a dimensionless form,

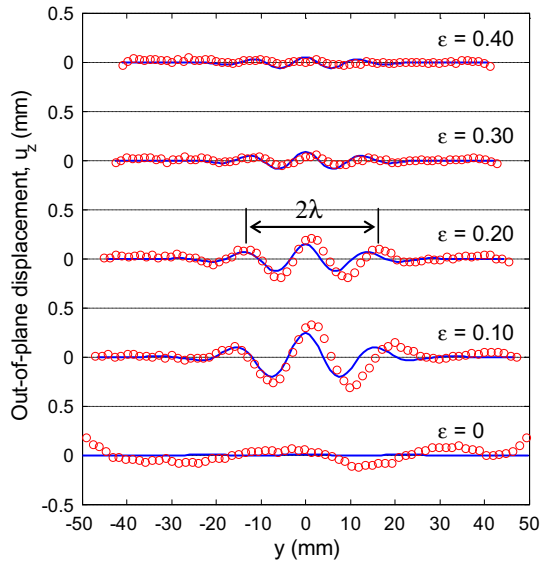


**Fig. 13.** Comparison of measured wrinkle profiles at different strain levels (symbols) with numerical simulations (lines) using the nonlinear viscoelastic PN model for the polyethylene specimen with  $\alpha = 2.5$  and  $\dot{\epsilon} = 0.0169 \text{ s}^{-1}$ .

$\lambda/W \sim (\alpha/\beta)^{1/2} \epsilon^{-1/4}$ , where  $\alpha = L/W$  and  $\beta = W/h$ . Fig. 15 shows the variation of the normalized wrinkle wavelength ( $\lambda/W_0$ ) vs. the dimensionless group  $(\alpha/\beta)^{1/2} \epsilon^{-1/4}$ , comparing the experimental measurements for the polyethylene sheets with the scaling analysis and numerical simulations. As seen in Fig. 3, with increasing nominal strain, the number of wrinkles remains nearly constant while the wrinkle wavelength decreases due to Poisson's contraction in the transverse direction. The wrinkle wavelength is measured as the average of the two peak-to-peak distances at the center of the profile, as shown in Fig. 13. It is found that the wrinkle wavelength is almost insensitive to the constitutive behavior of the material: the numerical simulations using three different material models (hyperelastic, HVE, and PN) are nearly indistinguishable in terms of the wrinkle wavelengths. This suggests that the wrinkle wavelength depends primarily on the geometry of the sheet (aspect ratios  $\alpha$  and  $\beta$ ) and the strain, while the wrinkle amplitude is more sensitive to the mechanical properties of the sheet material. As a result, the scaling analysis provides an accurate prediction for the wrinkle wavelength, but not for the wrinkle amplitude. As discussed by Healey et al. (2013), even for a linear elastic sheet, the wrinkle amplitude first increases and then decreases with increasing nominal strain as a result of a geometrically nonlinear coupling between the large in-plane strain and out-of-plane deflection. Qualitatively similar wrinkle evolution is predicted for hyperelastic and viscoelastic thin sheets, although the wrinkle amplitude depends quantitatively on the material model.

Finally we note that discrepancies between the experiments and the numerical simulations remain for several reasons. The initial undulation of the specimen is responsible for some of the discrepancies, particularly at relatively low strains. In addition, it is important to align the specimen precisely with the loading devices to avoid wrinkles induced by shearing or twisting. The clamped boundary conditions at both ends of the specimen is also challenging as the sheet could partly slide out of the clamps at large strains. Other experimental uncertainties may result from the non-uniformity of the polyethylene sheets. It was found that the thickness of the polyethylene sheet specimen could vary spatially up to  $10 \mu\text{m}$  from the nominal thickness of  $100 \mu\text{m}$  (Nayyar, 2013). Moreover, defects in the thin sheet material – such as inclusions – could affect the wrinkle profile. Localized wrinkles were observed in a polyethylene sheet stretched to about  $\epsilon \approx 0.9$  (Fig. 16(a)), due

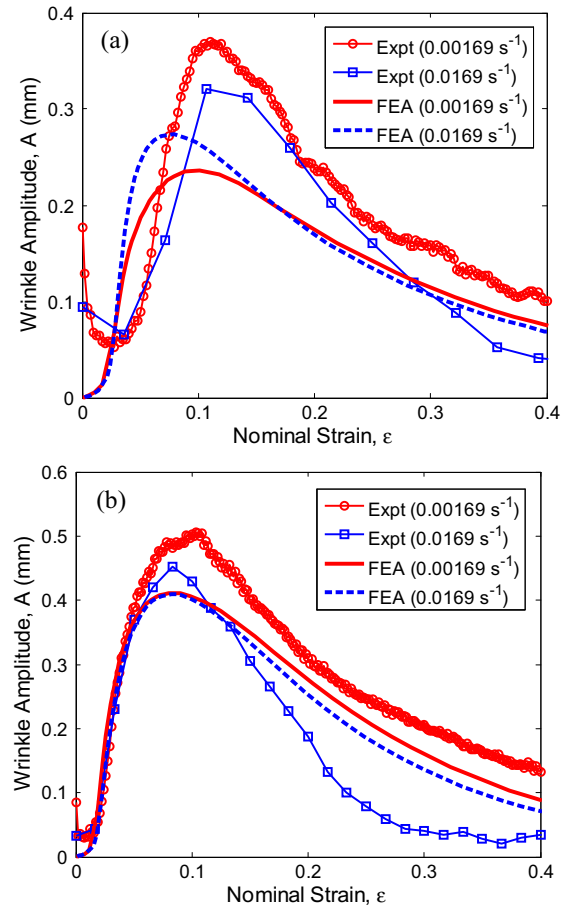


**Fig. 14.** Comparison of wrinkle amplitudes between experiments and numerical simulations using the nonlinear viscoelastic PN model for two aspect ratios: (a)  $\alpha = 2.5$ ; (b)  $\alpha = 2$ .

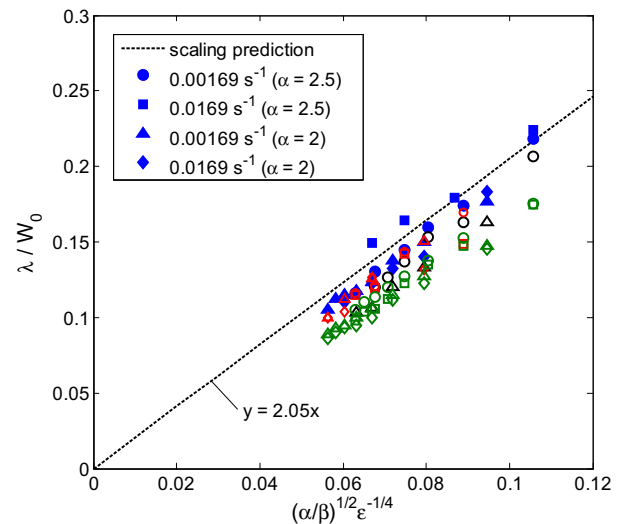


**Fig. 15.** Normalized wrinkle wavelength, comparing the measurements (filled symbols) with the scaling analysis (dashed line) and numerical simulations (open symbols). Data includes two aspect ratios,  $\alpha = 2$  and  $2.5$ , and two strain rates,  $\dot{\epsilon} = 0.0169$  and  $0.00169 \text{ s}^{-1}$ . Three different material models are used in the numerical simulations: hyperelastic (black), hyper-viscoelastic (green), and PN (red) models. The wavelength is measured or calculated at different strain levels for each specimen;  $\beta = 1000$  for all specimens. (For interpretation of the references to color in this figure legend, the reader is referred to the web version of this article.)

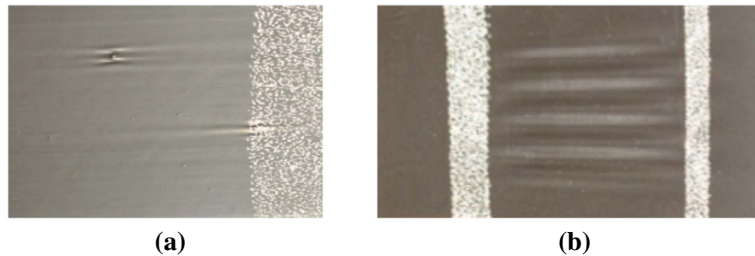


**Fig. 16.** (a) Optical image of a polyethylene sheet stretched to ~90% nominal strain, showing formation of localized wrinkles due to defects in the material; (b) stretch-induced wrinkling in a polyethylene sheet with localized plastic deformation.

to inclusion-like defects. The presence of such defects makes the wrinkling behavior less predictable at large strains. In Fig. 16(b), the polyethylene sheet appears to be locally thinned or otherwise altered in the painted region, possibly due to inhomogeneous plastic deformation, which resulted in an abnormal wrinkle pattern. In addition, from the numerical side, other constitutive models may be considered to further improve the simulations.

## 6. Summary

Stretch-induced wrinkle patterns in thin polyethylene sheets are measured experimentally using the three-dimensional digital image correlation technique. It is observed that the wrinkle amplitude first increases and then decreases with increasing nominal strain, in agreement with finite element simulations for a hyperelastic thin sheet. However, unlike the hyperelastic model, the stretch-induced wrinkles in the polyethylene sheet are not fully flattened at large strains ( $\epsilon > 0.3$ ). This is attributed to the nonlinear viscoelastic behavior of the material. Two experimentally calibrated viscoelastic material models – a hyper-viscoelastic model and a parallel network model – are used in numerical simulations to examine the effects of viscoelasticity on wrinkling. It is found that the parallel network model of nonlinear viscoelasticity is suitable for simulating the stretch-induced wrinkling of the polyethylene sheets. In general, while evolution of the wrinkle amplitude is quite sensitive to the mechanical properties of the sheet material, the wrinkle wavelength depends primarily on the geometry of the sheet (aspect ratios  $\alpha$  and  $\beta$ ) and the nominal strain.

## Acknowledgments

VN and RH gratefully acknowledge financial supports by National Science Foundation through Grant No. 0926851.

## References

- ABAQUS, 2012. ABAQUS Theory Manual and Analysis User's Manual (Version 6.12). Dassault Systèmes Simulia Corp., Providence, RI, USA.
- Ayoub, G., Zairi, F., Nait-Abdelaziz, M., Gloaguen, J.M., 2010. Modelling large deformation behavior under loading-unloading of semicrystalline polymers: application to a high density polyethylene. *Int. J. Plast.* 26, 329–347.
- Bergström, J.S., Boyce, M.C., 1998. Constitutive modeling of the large strain time-dependent behavior of elastomers. *J. Mech. Phys. Solids* 46, 931–954.
- Blandino, J.R., Johnston, J.D., Dharmasi, U.K., 2002. Corner wrinkling of a square membrane due to symmetric mechanical loads. *J. Spacecraft Rockets* 39, 717–724.
- Boyce, M.C., Socrate, S., Llana, P.G., 2000. Constitutive model for the finite deformation stress-strain behavior of poly(ethylene terephthalate) above the glass transition. *Polymer* 41, 2183–2201.
- Cerda, E., Mahadevan, L., 2003. Geometry and physics of wrinkling. *Phys. Rev. Lett.* 90, 074302.
- Cerda, E., Ravi-Chandar, K., Mahadevan, L., 2002. Wrinkling of an elastic sheet under tension. *Nature* 419, 579–580.
- Drozdzov, A.D., Gupta, R.K., 2003. Constitutive equations in finite viscoplasticity of semicrystalline polymers. *Int. J. Solids Struct.* 40, 6217–6243.
- Dusunceli, N., Colak, O.U., 2006. High density polyethylene (HDPE): experiments and modeling. *Mech. Time-Dependable Mater.* 10, 331–345.
- Friedl, N., Rammerstorfer, F.G., Fisher, F.D., 2000. Buckling of stretched strips. *Comput. Struct.* 78, 185–190.
- Healey, T.J., Li, Q., Cheng, R.B., 2013. Wrinkling behaviour of highly stretched rectangular elastic films via parametric global bifurcation. *J. Nonlinear Sci.* 23, 777–805.
- Jacques, N., Potier-Ferry, M., 2005. On mode localisation in tensile plate buckling. *C. R. Mec.* 333, 804–809.
- Jenkins, C.H., Haugen, F., Spicher, W.H., 1998. Experimental measurement of wrinkling in membranes undergoing planar deformation. *Exp. Mech.* 38, 147–152.
- Kim, T.Y., Puntel, E., Fried, E., 2012. Numerical study of the wrinkling of a stretched thin sheet. *Int. J. Solids Struct.* 49 (5), 771–782.
- Luo, P., Chao, Y., Sutton, M., Peters, W., 1993. Accurate measurement of three-dimensional deformations in deformable and rigid bodies using computer vision. *Exp. Mech.* 33, 123–132.
- Nayyar, V., 2013. Stretch-Induced Wrinkling in Thin Sheets (PhD dissertation). University of Texas at Austin, Austin, TX.
- Nayyar, V., Ravi-Chandar, K., Huang, R., 2011. Stretch-induced stress patterns and wrinkles in hyperelastic thin sheets. *Int. J. Solids Struct.* 48, 3471–3483.
- Orteu, J.J., 2009. 3-D computer vision in experimental mechanics. *Opt. Lasers Eng.* 47, 282–291.
- Puntel, E., Deseri, L., Fried, E., 2011. Wrinkling of a stretched thin sheet. *J. Elast.* 105, 137–170.
- Segedin, R.H., Collins, I.F., Segedin, C.M., 1988. The elastic wrinkling of rectangular sheets. *Int. J. Mech. Sci.* 30 (10), 719–732.
- Shim, V.P.W., Yang, L.M., Lim, C.T., Law, P.H., 2004. A visco-hyperelastic constitutive model to characterize both tensile and compressive behavior of rubber. *J. Appl. Polym. Sci.* 92, 523–531.
- Simo, J.C., 1987. On a fully three-dimensional finite-strain viscoelastic damage model: formulation and computational aspects. *Comput. Methods Appl. Mech. Eng.* 60, 153–173.
- Sutton, M.A., Orteu, J.-J., Schreier, H.W., 2009. Image Correlation for Shape, Motion and Deformation Measurements: Basic Concepts, Theory and Applications. Springer, New York.
- Wong, Y.W., Pellegrino, S., 2006. Wrinkled membranes. Part I: Experiments. *J. Mech. Mater. Struct.* 1, 1–23.
- Zheng, L., 2009. Wrinkling of Dielectric Elastomer Membranes (PhD dissertation). California Institute of Technology, Pasadena, CA.